# Theory of dynamical scattering in near-edge electron energy loss spectroscopy

C. Witte,[1] S. D. Findlay,[2] M. P. Oxley,[3,4] J. J. Rehr,[5] and L. J. Allen[1]
[1]*School of Physics, University of Melbourne, Parkville, Victoria 3010, Australia*
[2]*Institute of Engineering Innovation, School of Engineering, University of Tokyo, Tokyo 113-8656, Japan*
[3]*Department of Physics and Astronomy, Vanderbilt University, Nashville, Tennessee 37325, USA*
[4]*Materials Science and Technology Division, Oak Ridge National Laboratory, Oak Ridge, Tennessee 37831, USA*
[5]*Department of Physics, University of Washington, Seattle, Washington 98195, USA*
(Received 17 August 2009; revised manuscript received 21 October 2009; published 17 November 2009)

Beyond chemical information, the fine structure of an absorption edge gives bonding and electronic information. We provide a synthesis of fine structure and dynamical scattering theory, allowing the exploration of the effects of dynamical scattering on the measured fine structure. We discuss the effects of experimental geometry in the context of site-specific near-edge spectroscopy of $NiAl_2O_4$ and find that large detectors serve to localize the inelastic signal and may be preferable to the small off-axis detectors currently used. We then explore the possibility of measuring changes in fine structure within a unit cell using scanning transmission electron microscopy. We demonstrate that, in principle, it is possible to measure a subtle change in the fine structure of the O *K* edge in $SrTiO_3$ as the probe is scanned across the unit cell. We explore the best experimental conditions to achieve this and find that large probe-forming and detector apertures help to localize the signal to the atomic sites.

DOI: 10.1103/PhysRevB.80.184108 PACS number(s): 61.05.jd, 79.20.Uv

## I. INTRODUCTION

For determining materials properties on small length scales and in highly localized areas, transmission electron microscopy (TEM) is the technique of choice. Structural information is obtained from the configuration of columns in projection, which can be used to explore the distribution of dopants and defects and to analyze interfaces. Chemical information is obtained if the atomic species can be identified either through their atomic charge or through spectral identification. Scanning TEM (STEM) electron energy loss spectroscopy (EELS) has been used to image single-atom impurities within the bulk[1] and more recently has led to full two-dimensional chemical mapping at atomic resolution.[2–6] Functional properties of materials from atomic level can be analyzed if such properties as the atomic valence and bonding, and details about the conduction band can be measured. These last can be obtained from the fine structure in core-loss EELS, which arises from the interaction between the ejected electron and its local environment.[7,8] At some distance from threshold, the fine structure relates to the location and number of nearest neighbors of the ionized atom.[9] Near to the threshold, electron energy loss near-edge structure (ELNES) (approximately 0–50 eV above threshold) gives information about the local bonding environment[10] and the local projected unoccupied density of states.[11]

The theory of ELNES and the closely related technique of x-ray absorption NES (XANES) have been well explored.[7,11–15] Methods such as density-functional theory[16,17] and real-space multiple scattering[13,15,18] have been used successfully to calculate core-loss spectra. These calculations involve determining the wave function of the ejected electron as a function of the ejection energy. However they typically assume that the probing wave field is a plane wave. The generalization to include the influence of the scattering geometry, both that of the detector and of allowing for a convergent incident probe, has also been explored.[19–24] However this is only half the story for TEM since the crystal serves to significantly modify the incident wave field for all but the thinnest of specimens.

There are a number of ways in which the elastic or dynamical scattering of the fast electron which instigates the ionization events may interact with the fine structure and so impact upon the shape of the measured spectra. The symmetry of some crystals is such that certain atoms have different spectra associated with different symmetry axes. The weighting of these spectra then depends on the angular distribution of the incident and outgoing fast electrons, which is changed by elastic scattering. The material may have atoms of equivalent type but in different local environments, especially if dopants or interfaces are considered. In this case, the relative excitation of the different possible contributing spectra will depend on the distribution of the illuminating beam relative to these sites. This can be significantly changed by the elastic scattering prior to the ionization event. In some instances this might be regarded as a hindrance: probe spreading serving to slowly degrade the resolution. Some techniques take advantage of it, for instance, atom location by channeling-enhanced microanalysis (ALCHEMI).[25,26] Either way, a detailed understanding of the consequences of the elastic scattering of the fast electron wave function both before and after the ionization events is essential for any sort of quantitative analysis with this technique.

An explicit theory of ELNES including the dynamical scattering of the fast electron was first explored by Saldin.[27] Schattschneider *et al.*[28] presented the first calculations to explore the detailed coupling between channeling and fine-structure theory in the conventional TEM geometry. Recent experimental[29,30] and theoretical[31] work has explored the effects of dynamical scattering on ELNES in electron-diffraction spectroscopy. Site-specific electronic-structure analysis[29,30] was achieved but the effects of dynamical scattering were treated independently from the calculation of

 

ELNES spectra. The interplay between dynamical scattering and ELNES in this scenario has not been explored. We explore the effects of dynamical scattering on ELNES in electron-diffraction spectroscopy using $NiAl_2O_4$ as a case study and compare our simulations to recent experiments. In particular, we explore the parameters that provide optimal experimental conditions.

The mixed dynamical form factor (MDFF) approaches to energy loss simulation in TEM (Refs. 32–35) have implicitly contained the framework suitable for simulating both the channeling and the energy loss. Allen *et al.*[36] showed how to generalize such formulations to handle STEM probe incidence. But the results of such calculations have tended to be applied to cases where the total cross section after integration over an energy window is all that is required, and, since such integration tends to average out the fine-structure effects, such calculations have naturally been based on the energy loss spectra of isolated atoms because of the considerable computational simplification it offers.[37–39] STEM ELNES offers the prospect for recording atomic bonding maps.[5] However the interpretation of these will sensitively depend both on the delocalized nature of the ionization interaction[40,41] and on the dynamical spreading of the probe. The significance of the latter was appreciated by Möbus and Nufer,[42] who performed detailed dynamical scattering simulations of nanoprobe propagation. They then estimated ELNES signals by using this electron intensity to weight the local projected density of states, a reasonable first estimate but one which does not incorporate the details of the long-range nature of the ionization interaction, the phase of the fast electron wave function and the detector geometry, all of which are known to be important for EELS and have the potential to affect EELS images in nonintuitive ways.[41] Mizoguchi *et al.*[43] similarly recognized that the STEM ELNES signal would depend on the distribution of the probe in materials with atoms of the same type on inequivalent sites. That work determined the different spectra for the different sites but was unable to determine the weighting for a STEM probe scattering through a crystal. We therefore further generalize the approach to simulate in detail ELNES signals in STEM. We discuss the theory of STEM ELNES and, using $SrTiO_3$ as a case study, present calculations for STEM ELNES which include the dynamical scattering of the probe.

## II. BRIEF OVERVIEW OF ELECTRON ENERGY LOSS FINE STRUCTURE UNDER KINEMATIC CONDITIONS

Differentiating the well-known expression for the so-called kinematic cross section for inelastic scattering with respect to energy we have[38]

$$\frac{\partial\sigma(\mathbf{K})}{\partial E} = \frac{N}{2\pi^4 a_0^2 K}\int \frac{K'}{2}\sum_n \frac{M_n(\mathbf{q},\mathbf{q})}{|\mathbf{q}|^4} d\Omega_{K'}. \tag{1}$$

By kinematic we mean that this expression ignores the effects of dynamical scattering, i.e., it assumes that the fast electron wave function both before and after inelastic scattering can be described by plane waves. An incident plane wave with wave vector $\mathbf{K}$ is assumed. The sum over $n$ includes only those atoms of the species being ionized, $K'$ is the wave number of the inelastically scattered electron, $N$ is the number of unit cells in the sample, $a_0$ is the Bohr radius, and the scattering vector $\mathbf{q}=\mathbf{K}-\mathbf{K}'$. The MDFF of atom $n$ is[32,44]

$$M_n(\mathbf{q},\mathbf{q}',E) = \sum_{f,i} F^*_{n,fi}(\mathbf{q},E)F_{n,fi}(\mathbf{q}',E), \tag{2}$$

where the atomic transition-matrix element for a particular orbital is

$$F_{n,fi}(\mathbf{q},E) = \int u^*_{n,f}(E,\mathbf{r})e^{2\pi i\mathbf{q}\cdot\mathbf{r}}u_{n,i}(\mathbf{r})d\mathbf{r}. \tag{3}$$

Here $u_{n,i}$ and $u_{n,f}$ are the initial (bound) and final (continuum) state wave functions of the target electron of atom $n$. The wave function of the ejected electron depends on the energy loss $E$ of the fast electron, and it is this dependence which introduces the energy-dependent fine structure into the energy differential scattering cross section. When $\mathbf{q}=\mathbf{q}'$, as for the case of plane-wave scattering in Eq. (1), the MDFF reduces to the dynamic form factor which is the transition probability amplitude of the target being excited from state $i$ to $f$.

For an isolated atom, Eq. (3) can be evaluated in its entirety.[45] However, for the purposes of considering the fine structure, and, in particular, to make use of the output of existing fine-structure calculation packages, it is desirable at this point to make the dipole approximation for the exponential operator in Eq. (3). For conventional TEM this is thought to be an excellent approximation.[46–49] Using the orthogonality of the initial and final states,[15] and expanding the dot product in Cartesian form, Eq. (3) becomes

$$F_{n,fi}(\mathbf{q},E) = 2\pi i\sum_\alpha q_\alpha \int u^*_{n,f}(E,\mathbf{r})r_\alpha u_{n,i}(\mathbf{r})d\mathbf{r}, \tag{4}$$

where $r_\alpha$ and $q_\alpha$ are the $x$, $y$, or $z$ components of $\mathbf{r}$ and $\mathbf{q}$, respectively. Substituting this into Eq. (2) we get

$$M_n(\mathbf{q},\mathbf{q}',E) = 4\pi^2\sum_{\alpha,\beta} q_\alpha q'_\beta R_{n,\alpha\beta}(E), \tag{5}$$

where the $3\times 3$ matrix

$$R_{n,\alpha\beta}(E) = \sum_{f,i}\int u_{n,f}(E,\mathbf{r})r_\alpha u^*_{n,i}(\mathbf{r})d\mathbf{r} \times \int u^*_{n,f}(E,\mathbf{r}')r'_\beta u_{n,i}(\mathbf{r}')d\mathbf{r}'. \tag{6}$$

Depending on the symmetries of the sample, not all of the elements of $R_{\alpha\beta}$ will be nonzero and distinct. For example, take the oxygen $K$ edge in NiO. Due to the high symmetry of the crystal, $R_{\alpha\beta}$ is diagonal and all the diagonal elements are identical. For the lower-symmetry case where the atom is located on a threefold, fourfold, or sixfold rotational symmetry axis, the EELS cross section is dichroic.[22,50–55] In that case, if the main rotation axis is in the $z$ direction, then $R_{\alpha\beta}$ is diagonal and $R_{xx}=R_{yy}\neq R_{zz}$, i.e., the spectrum recorded

from the sample comprises some suitably weighted combination of two independent spectra, one associated with the plane of rotation and another associated with the axis of rotation. For still lower symmetries the sample can exhibit trichroism,[56–58] which has three, four, or six inequivalent spectra. One way that channeling can affect the measured fine structure is to change the weighting of these different spectra, as we will see in the following sections.

If we integrate over a sufficiently large energy window above the ionization threshold the effects of fine structure are averaged over and we can make an isolated atom approximation for the calculation of $R_{\alpha\beta}$. The upper limit of the energy window must be chosen such that the fine structure has damped down sufficiently at that point. An upper limit of tens of eV is usually acceptable but will vary depending on the sample used. Otherwise, more complicated methods are needed to include the effect of neighboring atoms on the final-state wave function. We use the real-space multiple scattering package FEFF (Refs. 13 and 59) to do this. FEFF is a cluster method based on real-space multiple-scattering theory that includes the effect of an energy-dependent self-energy and a screened core hole.[10] FEFF can calculate Eq. (6) including the effect of all atoms within a specific radius of the ionized atom. It is usually used in the calculation of XANES but, due to the correspondence between XANES and ELNES,[27] can also be used to calculate ELNES.

It is worth considering the computational complexity introduced into cross-section calculations by including the fine structure. $R_{\alpha\beta}(E)$ can have large oscillations, requiring a fine sampling in energy to accurately describe them. As identical atomic species can have different local environments, $R_{\alpha\beta}(E)$ must also be recalculated for the different possible local environments of the ionized atom. Additionally, for the ELNES case, the cross-section expression must be re-evaluated for every energy loss. This has necessitated the optimization of code used to calculate the differential cross section. In particular, the integration over the detector was highly optimized. Additionally, OPENMP (Ref. 60) was used to parallelize the code across multiple processors.

Previously it had been assumed that relativistically correcting the electron mass and wave vector were sufficient[61] for the typical energies used in electron microscopy, but it has recently been shown in magic-angle studies, aperture combinations which make the recorded spectra independent of sample orientation, that relativistic corrections to the transition-matrix elements are important.[53,54] These corrections were also proposed for the theory of STEM EELS (Ref. 62) and were required to achieve quantitative agreement between experiment and theory in core-loss convergent-beam electron diffraction.[63] To apply the correction we replace $\mathbf{q}$ and $\mathbf{r}$ in Eq. (5) by

$$\mathbf{q}' = \mathbf{q} - \frac{\beta^2(\mathbf{q}\cdot\mathbf{v})}{v}\hat{\mathbf{v}} \tag{7}$$

and

$$\mathbf{r}' = \mathbf{r} - \frac{\beta^2(\mathbf{r}\cdot\mathbf{v})}{v}\hat{\mathbf{v}}, \tag{8}$$

where $v$ is the magnitude of the velocity of the fast electron, $\mathbf{v}$, in direction $\hat{\mathbf{v}}$ and $\beta = v/c$ is the speed of the fast electron relative to the speed of light $c$. The net effect of this correction is a contraction of $\mathbf{q}$ and $\mathbf{r}$ in the direction of motion of the fast electron. These corrections have been included in all the following simulations.

## III. FINE STRUCTURE AND CHANNELING ASSUMING PLANE-WAVE INCIDENCE ON THE SPECIMEN

We now extend our theoretical development to include the elastic scattering of the fast electron both before and after the ionization event. Following Allen *et al.*[64] we assume a fast electron incident on a slablike specimen, where $\mathbf{r}_\perp$ is a vector in the plane of the surface of the sample and $z$ increases as the fast electron propagates through the sample. Following Allen *et al.*,[36] with a change to the $\mathcal{S}$-matrix notation of Fujimoto[65] and Sturkey,[66] we can describe the propagation of the elastic wave function in Fourier space as

$$\Psi_{\mathbf{G}}(\mathbf{K},z_2) = \sum_{\mathbf{H}} \mathcal{S}_{\mathbf{G},\mathbf{H}}(\mathbf{K},z=z_2-z_1)\Psi_{\mathbf{H}}(\mathbf{K},z_1), \tag{9}$$

where the elastic scattering matrix element $\mathcal{S}_{\mathbf{G},\mathbf{H}}(\mathbf{K},z)$ can be interpreted as the transition matrix element for elastic scattering from beam $\mathbf{K}+\mathbf{H}$ to $\mathbf{K}+\mathbf{G}$ over a thickness $z$. The Fourier coefficients at the entrance surface of the crystal, $\Psi_{\mathbf{H}}(\mathbf{K},0)$, can be found by requiring continuity of the wave function at the surface of the crystal. For plane-wave illumination $\Psi_{\mathbf{H}}(\mathbf{K},0)=\delta_{\mathbf{H},\mathbf{0}}$ and hence

$$\Psi_{\mathbf{G}}(\mathbf{K},z) = \sum_{\mathbf{H}} \mathcal{S}_{\mathbf{G},\mathbf{H}}(\mathbf{K},z)\,\delta_{\mathbf{H},\mathbf{0}} = \mathcal{S}_{\mathbf{G},\mathbf{0}}(\mathbf{K},z). \tag{10}$$

Separating the sum over final states $p$ in the inelastic cross section of Allen *et al.*[64] to an integral over energy $dE$ and a sum over final states for a fixed energy, the energy differential inelastic cross section can be written as

$$\begin{aligned}\frac{\partial\sigma(\mathbf{K},t)}{\partial E} = NV_c\frac{2m}{\hbar^2K}\int \sum_{\mathbf{G},\mathbf{H},\mathbf{G}',\mathbf{H}'} \frac{1}{t}\int_0^t \mathcal{S}_{\mathbf{G},\mathbf{0}}(\mathbf{K},z)\mathcal{S}^*_{\mathbf{H},\mathbf{0}}(\mathbf{K},z)\\ \times \mathcal{S}_{\mathbf{0},\mathbf{G}'}(\mathbf{K}',t-z)\mathcal{S}^*_{\mathbf{0},\mathbf{H}'}(\mathbf{K}',t-z)dz\\ \times \frac{K'}{2}X_{\mathbf{H}-\mathbf{H}',\mathbf{G}-\mathbf{G}'}(\mathbf{K},\mathbf{K}',E)d\Omega_{K'}.\end{aligned} \tag{11}$$

Here $\mathbf{K}'$ is the wave vector of the fast electron after the ionization event and the integral $d\Omega_{K'}$ is over the solid angle of the vector $\mathbf{K}'$ consistent with the detector. This expression includes dynamical scattering of the fast electron both before and after the ionization event, so-called double channeling. The transition matrix element for elastic scattering from beam $\mathbf{K}+\mathbf{0}$ to $\mathbf{K}+\mathbf{G}$ through a depth $z$ of crystal is $\mathcal{S}_{\mathbf{G},\mathbf{0}}(\mathbf{K},z)$, $\mathcal{S}_{\mathbf{0},\mathbf{G}'}(\mathbf{K}',t-z)$ is the transition matrix element for elastic scattering after the ionization event at depth $z$ from $\mathbf{K}'+\mathbf{G}'$ to $\mathbf{K}'+\mathbf{0}$ in a thickness $t-z$, and similarly for the complex conjugates. The inelastic-scattering matrix,

$$\begin{aligned}&X_{\mathbf{H}-\mathbf{H}',\mathbf{G}-\mathbf{G}'}(\mathbf{K},\mathbf{K}',E)\\ &= \sum_n \mathcal{F}_n \frac{\hbar^2}{4\pi^4 m a_0^2}\frac{M_n(\mathbf{q}+\mathbf{H}-\mathbf{H}',\mathbf{q}+\mathbf{G}-\mathbf{G}',E)}{|\mathbf{q}+\mathbf{H}-\mathbf{H}'|^2|\mathbf{q}+\mathbf{G}-\mathbf{G}'|^2},\end{aligned} \tag{12}$$

connects these two elastic scattering processes. The MDFF

$M_n(\mathbf{q}+\mathbf{H}-\mathbf{H}',\mathbf{q}+\mathbf{G}-\mathbf{G}',E)$ is given in Eq. (2), and

$$\mathcal{F}_n = e^{-0.25B_n(\mathbf{G}-\mathbf{G}'-\mathbf{H}+\mathbf{H}')}e^{2\pi i(\mathbf{G}-\mathbf{G}'-\mathbf{H}+\mathbf{H}')\cdot\tau_n} \tag{13}$$

is similar to the site term of Allen *et al.*[64] but excludes the sum over atoms in the unit cell. The atomic sites of the species being ionized within the unit cell of volume $V_C$ are $\tau_n$ and the temperature factors $B_n(\mathbf{G})=8\pi^2\langle u_n^2\rangle G^2$, where $\langle u_n^2\rangle$ is the projected mean-square thermal displacement. Due to our separation of the sum over final states $p$ into an integral over energy and a sum over final states for a fixed energy, this expression has a subtle difference from the similar expression in Allen *et al.*:[64] here $X$ includes the sum over final states $f$ which was not included in $X$ in the earlier work.

Equation (11) describes dynamical scattering. It models scattering from the elastic beam to an inelastic beam as determined by the inelastic-scattering coefficient $X_{\mathbf{H}-\mathbf{H}',\mathbf{G}-\mathbf{G}'}$. Thermal scattering is included as an effective absorption, attenuating the electron density in the elastic beams, both before and after the ionization event. The electrons which are thus removed from our calculations can, in practice, still cause ionization events and so contribute to the scattering cross section. This was handled by a term describing diffuse scattering in Ref. 67. In the present work, that term describing diffuse scattering will be ignored as an unnecessary complication, though it can play a significant role for thick and strongly scattering specimens.[38] Effectively this means we are making a single elastic-to-inelastic transition approximation.[68]

In the cross-section expression in Eq. (11) we find that the $\mathcal{S}$ matrices occur in bilinear forms, which, not coincidentally, are strongly reminiscent of the density-matrix formulation.[44,69] The inelastic-scattering matrix elements are a function of two variables. In the cross-section expression of Eq. (11) the products with the $\mathcal{S}$ matrices occur in such a way as to be sensitive to phase effects, both in the probing wave field and in the self-interference of the various inelastic final states propagating out toward the detector plane. In the derivation of Allen and Josefsson,[38] the inelastic-scattering matrix elements turn up in the form of an effective scattering potential, and there the two variable dependence is described, based on the mathematical structure of the equations, in terms of nonlocality. In the context of imaging, this effective nonlocality prevents us from simply interpreting structure in images as structure in the specimen. This can lead to counterintuitive results such as imaging at a distance.[41] However, in some cases, due to the nature of the scattering and/or the geometry of the experiment, it suffices to approximate this nonlocal potential with an effective local potential.[70] One such case is plane-wave illumination, ignoring the dynamical scattering of the fast electron, as described by Eq. (1). Alternatively, it has been shown that for sufficiently large detector acceptance angles the imaging is based upon a local potential.[70] In the local approximation all that matters is the magnitude of the wave function. We are not sensitive to phase information and this is then termed an "incoherent" imaging model. Interpretation is greatly simplified in such a case.

To use Eq. (11) to evaluate the ELNES fine structure, we use the dipole approximation form, Eq. (4), of the mixed dynamic form factor appearing in Eq. (12). If we further restrict our attention only to the energy differential cross section for $K$-shell losses (not of necessity but merely for simplicity of notation), Eq. (11) becomes

$$\begin{aligned}\frac{\partial\sigma(\mathbf{K},t)}{\partial E} = {} & \frac{NV_c}{K\pi^2a_0^2}\sum_{n,\alpha,\beta}R_{n,\alpha\beta}(E) \\ & \times \sum_{\mathbf{G},\mathbf{H},\mathbf{G}',\mathbf{H}'}\frac{1}{t}\int\int_0^t \mathcal{S}_{\mathbf{G},\mathbf{0}}(\mathbf{K},z)\mathcal{S}^*_{\mathbf{H},\mathbf{0}}(\mathbf{K},z) \\ & \times \mathcal{S}_{\mathbf{0},\mathbf{G}'}(\mathbf{K}',t-z)\mathcal{S}^*_{\mathbf{0},\mathbf{H}'}(\mathbf{K}',t-z)dz \\ & \times K'\mathcal{F}_n\frac{(\mathbf{q}+\mathbf{H}-\mathbf{H}')_\alpha(\mathbf{q}+\mathbf{G}-\mathbf{G}')_\beta}{|\mathbf{q}+\mathbf{H}-\mathbf{H}'|^2|\mathbf{q}+\mathbf{G}-\mathbf{G}'|^2}d\Omega_{K'}.\end{aligned} \tag{14}$$

In principle, the shape of the spectra $R_{n,\alpha\beta}(E)$ can be modified by the energy dependence of $\mathbf{q}$ and the scattering matrices for the final-state electrons, but this effect is very weak for the typical range of energies investigated in ELNES experiments. The main effect of dynamical scattering on ELNES spectra is as a weighting of the spectra $R_{n,\alpha\beta}(E)$ dependent on the specific dynamical scattering conditions and experimental geometry. For instance, with a dichroic material the two spectra are weighted differently as the sample is tilted relative to the incident beam and detector. Dynamical scattering can also strongly affect the ELNES when the crystal studied has identical atomic species on inequivalent lattice sites. As the atoms on distinct sites have different local environments, they have differing energy loss spectra. By changing the dynamical scattering conditions we can alter the density of the probe electron around the different lattice sites and hence change the measured energy spectrum.

## IV. CASE STUDY: ELECTRON-DIFFRACTION SPECTROSCOPY OF $NiAl_2O_4$

### A. Atom location by channeling-enhanced microanalysis

ALCHEMI has been used to locate atomic species on different atomic sites within a unit cell[25,26] and the theory has been studied extensively.[37,71] Specific dynamical scattering conditions are used to concentrate the probe density on specific columns in the unit cells. With a sufficient understanding of the dynamical scattering and energy-dispersive x-ray emission spectroscopy measurements, ALCHEMI can be used to identify atomic species and their concentration at different sites within the unit cell.

Experiments have been performed under similar dynamical scattering conditions using an EELS detector,[72] allowing site-specific valence determination. Further experiments[73] extended this to look at fine structure at specific sites, allowing one to separate out the fine structure from identical atomic species on different lattice sites.[29–31,74] While the dynamical scattering theory and fine-structure theory of the experiments have been studied in isolation, a detailed analysis of the interplay between the two is an essential part of the

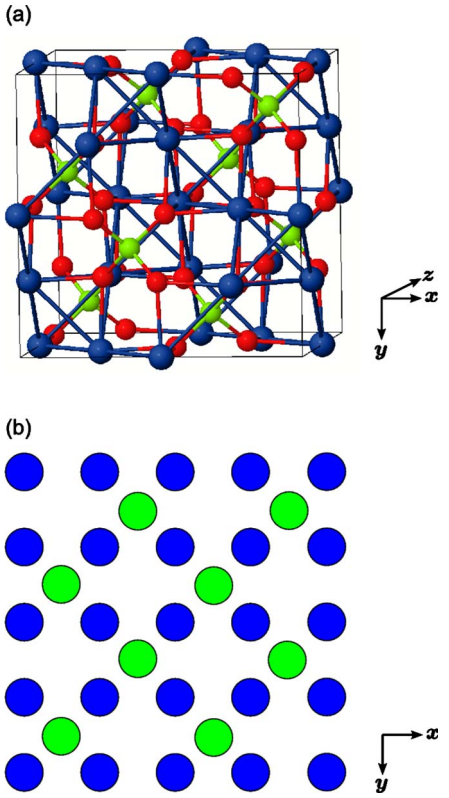


FIG. 1. (Color online) (a) The conventional unit cell of the spinels, with general structure $AB_2X_4$, produced using JMOL (Ref. 75). The $A$ atoms are in light gray (green) (tetrahedral sites), $B$ atoms are in dark gray (blue) (octahedral sites), and $X$ atoms are in medium gray (red). (b) The projection of the conventional unit cell of $NiAl_2O_4$ along [001]. It can be seen that the atoms form an $ABAB'ABAB'$ stacking sequence on the set of ⟨800⟩ planes.

physics and must be considered, particularly if the quantitative benefits of ALCHEMI are to be realized with EELS signals. Using nickel aluminate spinel ($NiAl_2O_4$) as a case study, we will explore this complex interaction.

### B. Structure of $NiAl_2O_4$

The spinel structure is well known,[76] having the general formula $AB_2X_4$ where $A$ and $B$ are cations and $X$ is an anion. Four primitive tetragonal unit cells can be combined to form the conventional cubic unit cell. In a normal spinel the $A$ cations occupy tetrahedral interstices of the anion lattice while the $B$ cations occupy octahedral interstices. The conventional unit cell is illustrated in Fig. 1(a). The tetrahedral ($A$) site has point symmetry $\bar{4}3m$ and belongs to the $T_d$ cubic point group. As such it has an isotropic EELS cross section in the dipole approximation. The octahedral ($B$) site has point symmetry $\bar{3}m$ (Ref. 76) and belongs to the $D_{3d}$ trigonal point group and as such has a dichroic[58] dipole ELNES cross section. The prototype for this class of crystals is the mineral spinel $MgAl_2O_4$. In a 2–3 spinel (composed of divalent and trivalent cations) the $A$ cation is divalent and the $B$ cation is trivalent.

In a completely inverse 2–3 spinel, the tetrahedral sites are populated by the trivalent cation and the octahedral sites

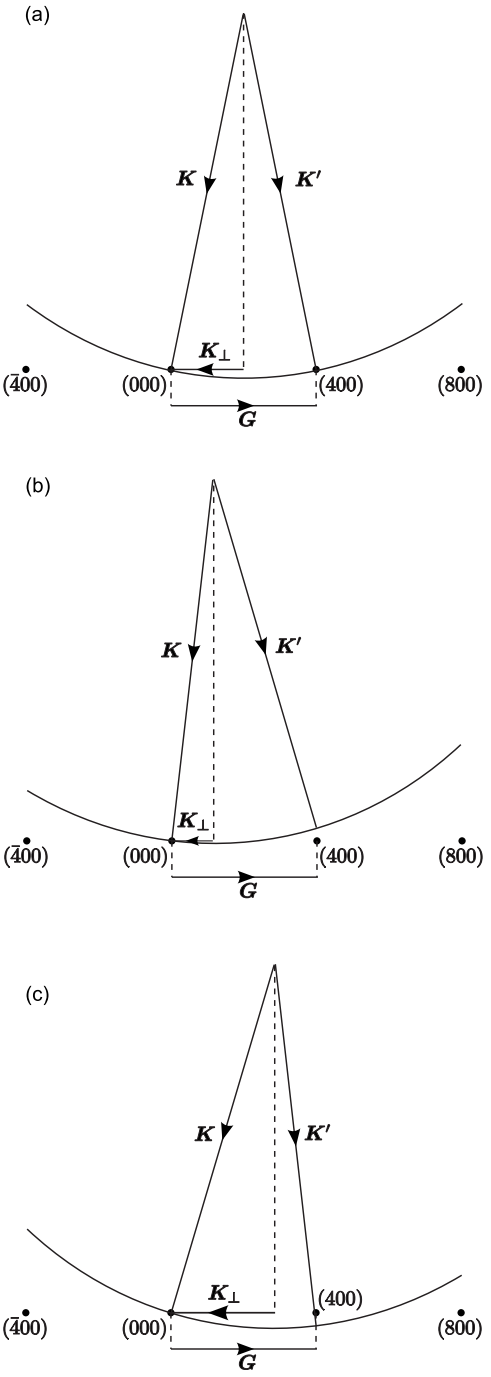


FIG. 2. The Ewald sphere in relation to the systematic row (a) in the exact Bragg condition where $\mathbf{K}_\perp = -0.5 \times \mathbf{G}$ (designated zero orientation elsewhere), (b) for orientations where the sample has been tilted to concentrate the probe on the tetrahedral site (designated positive), and (c) for orientations where the sample has been tilted to concentrate the probe on the octahedral site (designated negative).

are occupied by a mix of divalent and trivalent cations. Between these two extremes there exist partially inverse spinels. They are characterized by the degree of inversion $x$. $NiAl_2O_4$ is a partially inverse spinel where the degree of inversion is approximately $x \approx 0.8$.[77] For this case we have a significant number of Al atoms on both the tetrahedral and

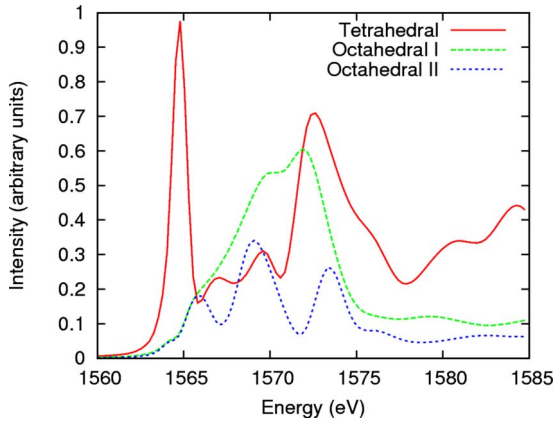


FIG. 3. (Color online) Calculations for the Al $K$ shell in $NiAl_2O_3$ done using FEFF of $R_{\alpha\beta}$ for the tetrahedral and octahedral sites.

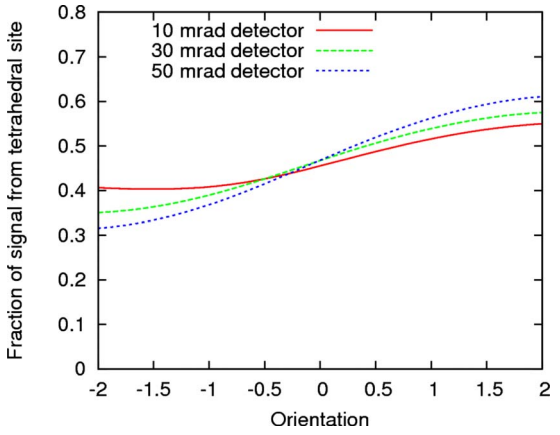


FIG. 4. (Color online) Fraction of signal from the tetrahedral site as a function of orientation of the sample about the (004) excitation for a range of detector sizes. The perpendicular component of the incident wave vector is given by $\mathbf{K}_\perp = -0.5a \times (100) + (200)$, where $a$ is the orientation on the horizontal axis. This means the 0 orientation is the exact (400) Bragg excitation. The sample thickness is 300 Å.

octahedral sites, i.e., we have identical atomic species with different local environments.

In Fig. 1(b) we see the projected structure of the conventional unit cell of $NiAl_2O_4$. It can be seen that the octahedral and tetrahedral sites alternate in an $ABAB'ABAB'$ fashion on the set of $\langle 800 \rangle$ planes.[29] Under systematic row conditions, where we are not sensitive to the change in potential in the vertical direction in Fig. 1(b), this reduces to an $ABABABAB$ stacking. Illuminating the sample with a plane wave, we can then tilt the sample to excite the (400) beam. Rocking either side of this excitation along the systematic row concentrates the probe on either the tetrahedral or octahedral sites.[29,31,72] Shifting the EELS detector off axis further improves the site selectivity.[72] In Fig. 2(a) we depict the Ewald sphere in relation to the systematic row for the exact Bragg condition. In this orientation $\mathbf{K}_\perp = -0.5 \times \mathbf{G}$, which we have designated as zero orientation. In Fig. 2(b) we depict the Ewald sphere for what we have called positive orientations, where the sample has been tilted away from the exact Bragg position to concentrate the probe on the tetrahedral sites and Fig. 2(c) depicts negative orientations where the probe is concentrated on the octahedral sites.

Using a $\beta$ version of FEFF 9,[13,59] electron-diffraction spectra were calculated for the Al $K$ edge in $NiAl_2O_4$. Full multiple scattering was included for an 8 Å cluster around the ionized atom with the potentials calculated self-consistently within a radius of 6.5 Å. In Fig. 3 we can see the calculated EELS spectra, $R_{\alpha\beta}$, in the dipole approximation for Al atoms on the tetrahedral site and the two spectra from the octahedral site. The tetrahedral EELS spectrum exhibits a large pre-edge peak that is absent from the octahedral spectrum. This feature, in particular, allows us to discriminate the signal from the tetrahedral and octahedral sites.

To get a feel for the effects of dynamical scattering we can examine a simplified case. Rather than looking at the details of the fine structure we can simply look at the relative signal of the Al $K$ edge originating from the different lattice sites. In this case it suffices to only look at one energy, the threshold energy. This is valid because the major effect of the channeling here is simply to weight the spectra arising at the different sites. Note that, within the dipole approximation, our calculations fully include the description of the ionization interaction. In particular, and contrary to previous studies which have sought just to assess the spatial distribution of the elastically scattered electrons, this approach correctly handles the so-called nonlocality of the inelastic matrix elements,[41] which mathematically describes the long-range nature of the ionization interaction and the partial coherence of the inelastically scattered wave field as it affects the signal reaching the detector. In the following calculations, done for an incident-beam energy of 200 keV, it was found that seven beams $[(\bar{1}200),(\bar{8}00),(\bar{4}00),(000),(400),(800),(1200)]$ were adequate to describe the dynamical scattering and runs on a standard desktop computer in tens of minutes. First we will explore the effects of detector size, then the detector offset and, finally, sample thickness.

### C. Effect of detector size

In Fig. 4 the fraction of the signal from a 300-Å-thick specimen for the tetrahedral site is plotted for a range of detector sizes as a function of sample tilt. (For the largest detectors shown here the validity of the dipole approximation may be questionable but for qualitative results should suffice.) The perpendicular component of the incident wave vector is given by $\mathbf{K}_\perp = -0.5a \times (100) + (200)$, where $a$ is the orientation on the horizontal axis. This means that (400) is in the Bragg condition and strongly excited at the 0 orientation.

A small detector aperture in the forward direction collects predominantly small-angle scattering. Loosely speaking, small-angle scattering corresponds to a large impact parameter and as such admits contributions from scattering events triggered by electrons passing at some distance from the target atoms. Given the long-range nature of this interaction, we therefore expect to see little change in the EELS spectra as a function of probe tilt. This is borne out in these simulations: for the smallest detectors, there is little change as we tilt the

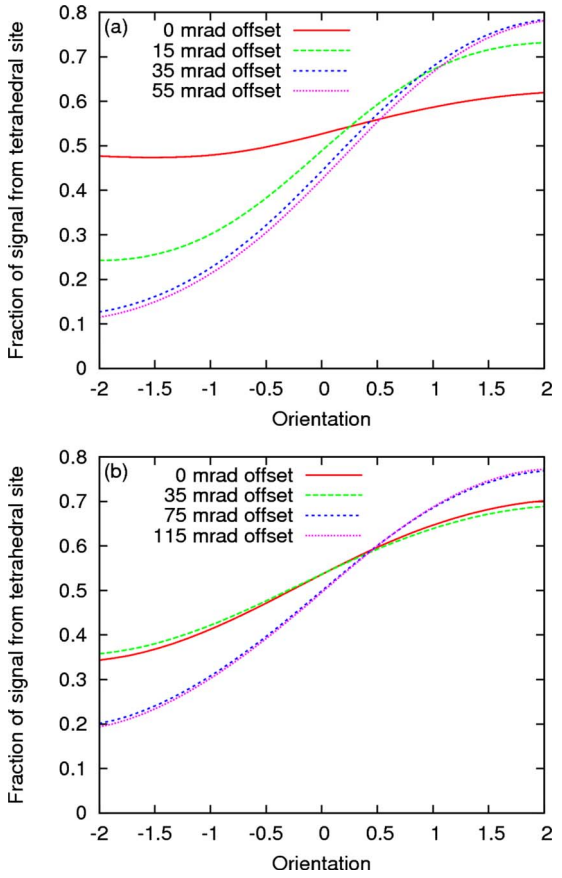


FIG. 5. (Color online) Fraction of the signal from the tetrahedral site as a function of sample orientation about the (004) excitation for (a) a 10 mrad and (b) a 50 mrad detector for a range of offsets. The perpendicular component of the incident wave vector is given by $\mathbf{K}_\perp = -0.5a \times (100) + (200)$, where $a$ is the orientation on the horizontal axis. The sample thickness is 300 Å.

probe around the (400) reflection excitation. For large detectors we find that for tilts toward the (000) beam (negative orientation) the signal from the tetrahedral site decreases and for tilts away (positive orientation) it increases.

### D. Effect of detector offset

We can explore the effect of offsetting the detector perpendicular to the systematic row direction when using a 200 keV incident beam, as in Tatsumi *et al.*[30] and Yamamoto *et al.*[29] In Fig. 5(a) we see that offsetting a 10 mrad detector leads to a large change in signal from the tetrahedral site as the sample, assumed to be 300 Å thick, is tilted. For a small offset of 5 mrad there is little change in the signal. As we increase the offset to 35 mrad we see a large change with the fraction of the signal from the tetrahedral site changing from about 0.1 for negative tilts to more than 0.7 for positive tilts. Increasing the detector offset beyond this range only marginally increases the change in the signal.

As can be seen in Fig. 5(b), for a larger detector of 50 mrad a much greater offset is needed to see the same change in the signal as we tilt the sample. In fact, even for offsets of 115 mrad we do not get as large a change in signal as for a detector with an acceptance angle of 10 mrad.

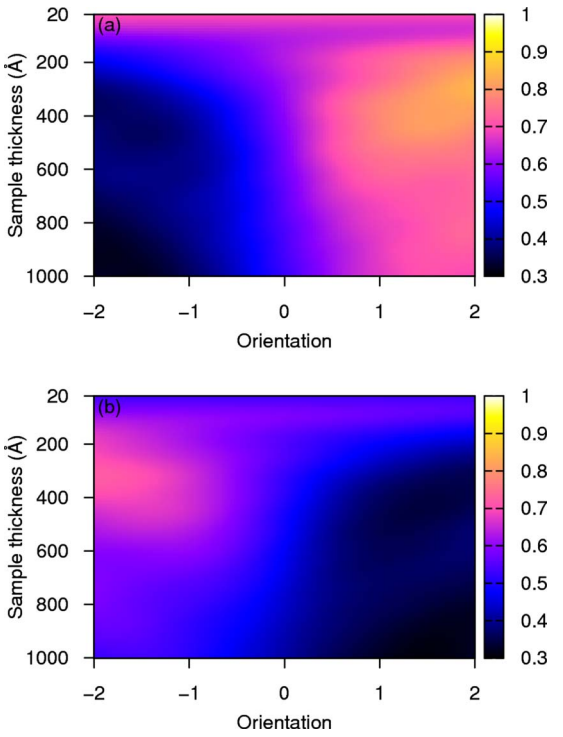


FIG. 6. (Color online) Strength of the Al $K$-edge signal from the (a) tetrahedral site and (b) octahedral site as a function of orientation and sample thickness for a 50 mrad detector. The perpendicular component of the incident wave vector is given by $\mathbf{K}_\perp = -0.5a \times (100) + (200)$, where $a$ is the orientation on the horizontal axis.

It is interesting to note that offsetting the detector produces a larger change in the signal as we tilt the sample than using a large on axis detector, thus favoring the small off-axis detector. How this behavior arises is obscured by the nonlocal interaction and detailed simulations are required to accurately model this effect. In practice the high count rate of the large on-axis detector will have to be balanced against the greater change in signal as a function of tilt of the small off-axis detector.

### E. Effect of sample thickness

At the surface of the crystal the probe is a plane wave with a uniform intensity across the surface. This means there is no change in signal per atom from either the tetrahedral or octahedral sites for thin crystals as we tilt the specimen. As the probe channels it concentrates on different atomic columns depending on the sample tilt. For negative tilts (toward the symmetric orientation) the probe concentrates on the octahedral site and for positive tilts the tetrahedral site. The effects of this can be seen in Fig. 6(a), which displays the signal per atom from the tetrahedral site as a function of orientation and thickness, and (b) which displays the signal per atom from the octahedral site. In both cases a 50 mrad detector is used. Initially the signal is independent of tilt. Then, as the probe starts to concentrate around the atomic columns, the signal becomes highly dependent on tilt.

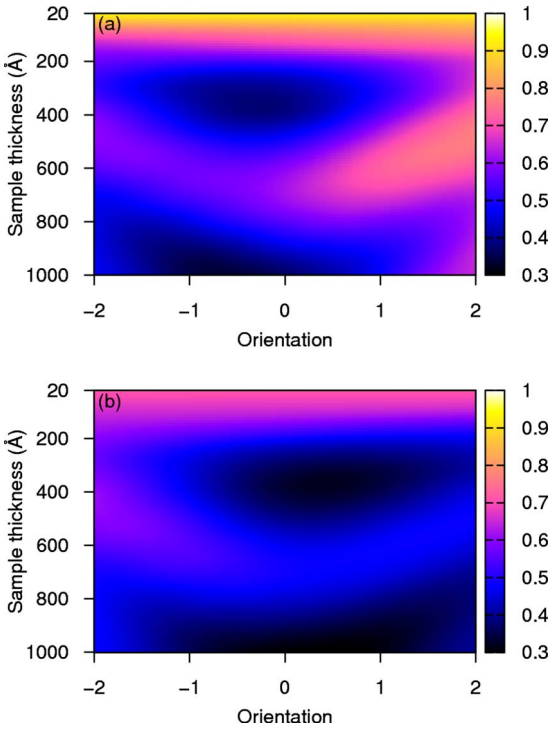


FIG. 7. (Color online) Strength of the Al *K*-edge signal from the (a) tetrahedral site and (b) octahedral site as a function of orientation and sample thickness for a 10 mrad detector. The perpendicular component of the incident wave vector is given by $\mathbf{K}_\perp = -0.5a \times (100) + (200)$, where $a$ is the orientation on the horizontal axis.

For a positive tilt, there is a maximum in intensity from the tetrahedral site at approximately 300 Å. The converse is true for the octahedral site. This signal per atom then slowly drops off as the inelastically scattered electrons undergo thermal scattering and are absorbed from the beam. These electrons add to a diffuse background[67] that has not been modeled here. For such a large detector the effects of dynamical scattering after the ionization event can be ignored. As can be seen in Fig. 7, for a 10 mrad detector the result is quite different. The failure of the single-scattering approximation makes the interpretation of experiment for a small on-axis detector more difficult as oscillatory features make the result highly dependent on sample thickness, an experimental parameter, that is, usually difficult to determine.

### F. Results

Using the $R_{\alpha\beta}$ spectra calculated by FEFF, the full double-channeling cross section including fine structure was simulated from first principles. The calculation was found to converge using seven beams. A thickness of 300 Å was used to maximize the difference in the spectra as a function of orientation.

In Fig. 8 we see the result of the simulations for a 50 mrad detector. There is a clear change in the fine structure as a function of probe tilt. The most noticeable change is that as we tilt from a positive to a negative orientation the second peak at approximately 1570 eV, associated with the octahedral site (peak B in Fig. 8), increases in size. The peak at approximately 1565 eV (peak A in Fig. 8), associated with the tetrahedral site, decreases as we tilt from positive to negative orientation. The signal from the tetrahedral site is noticeably weaker due to the fact there are three Al atoms on octahedral sites for every two Al atoms on tetrahedral sites.

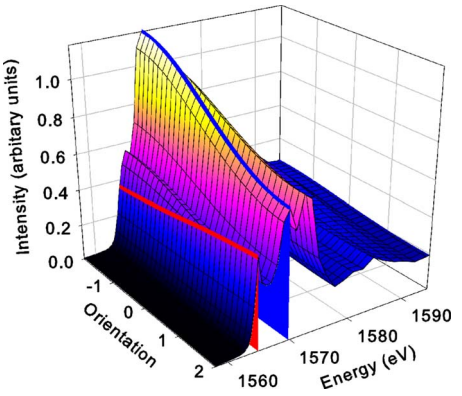


FIG. 8. (Color online) Full double-channeling ELNES calculation of the Al *K* edge in $NiAl_2O_4$ as a function of orientation and energy loss using a 50 mrad on-axis detector. Peaks A and B are indicated by the red and blue traces, respectively. The perpendicular component of the incident wave vector is given by $\mathbf{K}_\perp = -0.5a \times (100) + (200)$, where $a$ is the orientation on the horizontal axis.

In Fig. 9 we see the results for a similar simulation but with a 0.9 mrad detector offset by 12.5 mrad perpendicular to the (400) beam and a 700-Å-thick sample. These parameters were chosen to match the experimental conditions used by Yamamoto *et al.*[29] It is evident that the change in the signal from the octahedral site is much greater than for the 50 mrad detector (it should be noted that the 50 mrad on-axis detector has a signal strength approximately 100 times larger than the 10 mrad off-axis detector).

These results compare favorably with recent experiments.[29,30] As the experiments were not performed on

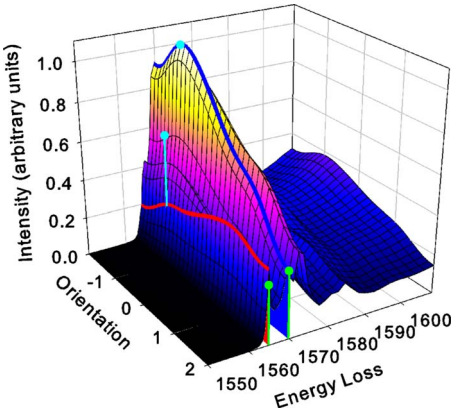


FIG. 9. (Color online) Full double-channeling ELNES calculation of the Al *K* edge in $NiAl_2O_4$ as a function of orientation and energy loss using a 0.9 mrad detector offset by 12.5 mrad. Peaks A and B are indicated by the red and blue trace, respectively. The perpendicular component of the incident wave vector is given by $\mathbf{K}_\perp = -0.5a \times (100) + (200)$, where $a$ is the orientation on the horizontal axis. Four experimental values from Ref. 29 are shown by the green and light blue dots, with the drop lines guiding the eye, as described in the text.

an absolute scale they can only inform us about the relative heights of peaks A and B. They observe the same enhancement of peak A relative to peak B for positive orientations. In Fig. 9 corresponding experimental peak heights (scaled to the theoretical peak B) and locations (after correcting for a small shift in energy) from Yamamoto *et al.*[29] are indicated for two different orientations of the sample. As the exact orientations are not given we assumed they are those that maximize the difference in the heights of peaks A and B, as for their previous work.[30] While the relative peak locations are accurately reproduced, the relative peak heights are not.

## V. FINE STRUCTURE AND CHANNELING ASSUMING CONVERGENT PROBE INCIDENCE ON THE SPECIMEN

As shown by Kirkland *et al.*[78] and Allen *et al.*,[36] the simulation of the fast electron wave function in STEM is simply a question of changing the incident boundary conditions. For STEM probe illumination, Eq. (10) becomes

$$\Psi_{\mathbf{g}}(\mathbf{R},z)=\sum_{\mathbf{h}}\mathcal{S}_{\mathbf{g},\mathbf{h}}(\mathbf{K},z)\Psi_{\mathbf{h}}(\mathbf{R},0), \tag{15}$$

where now

$$\Psi_{\mathbf{h}}(\mathbf{R},0)=T(\mathbf{h})e^{-2\pi i\mathbf{h}\cdot\mathbf{R}}, \tag{16}$$

in which $\mathbf{R}$ denotes the position of the STEM probe. The contrast transfer function,[79]

$$T(\mathbf{p})=A(\mathbf{p})\exp\left[-\frac{2\pi i}{\lambda}\chi(\mathbf{p})\right], \tag{17}$$

describes a focused collapsing spherical wave in reciprocal space. The objective aperture pupil function is

$$A(\mathbf{p})=\begin{cases}0, & \text{if } p>p_{\max}\\ 1, & \text{if } p\le p_{\max},\end{cases} \tag{18}$$

where $p_{\max}$ can be related to the aperture semiangle via $\alpha=\tan^{-1}(p_{\max}/k_0)\approx p_{\max}/k_0$. The phase distortion $\chi(\mathbf{p})$ models the path difference that off-axis waves experience due to lens aberrations. For a cylindrically symmetric lens with defocus $\Delta f$ (where an over focus is positive), third-order spherical aberration coefficient $C_3$ and fifth-order spherical aberration coefficient $C_5$,

$$\chi(\mathbf{p})=\frac{1}{2}\Delta f(\lambda p)^2+\frac{1}{4}C_s(\lambda p)^4+\frac{1}{6}C_5(\lambda p)^6. \tag{19}$$

There are some subtle differences between Eqs. (10) and (15). The Fourier coefficients of the fast electron wave function $\Psi$ are now a function of the probe position $\mathbf{R}$. The probe no longer has the same translational symmetry that the sample has, yet periodicity is implicitly assumed in Eqs. (15) and (16) through the use of a finite array of mesh points. We can eliminate the consequences of this spurious repetition of the probe by using a supercell large enough to prevent the repeated probes interacting with one another. The reciprocal space lattice vectors $\mathbf{g}$ are constructed on this supercell in contrast to the *physical* reciprocal-lattice vectors $\mathbf{G}$ used previously, which were derived from the conventional unit cell. The vectors $\mathbf{g}$ sample reciprocal space much more finely than the vectors $\mathbf{G}$.

The generalization of the energy differential inelastic cross section, Eq. (16), for STEM probe incidence is

$$\begin{aligned}\frac{\partial\sigma(\mathbf{R},t)}{\partial E}=NV_c\frac{2m}{\hbar^2K}\int\sum_{\mathbf{g}',\mathbf{h}',\mathbf{g}'',\mathbf{h}''}\frac{1}{t}\int_0^t\sum_{\mathbf{g},\mathbf{h}}&\\ \times\mathcal{S}_{\mathbf{g}',\mathbf{g}}(\mathbf{K},z)T(\mathbf{g})e^{-2\pi i\mathbf{g}\cdot\mathbf{R}}&\\ \times\mathcal{S}^*_{\mathbf{h}',\mathbf{h}}(\mathbf{K},z)T^*(\mathbf{h})e^{2\pi i\mathbf{h}\cdot\mathbf{R}}&\\ \times\mathcal{S}_{\mathbf{0},\mathbf{g}''}(\mathbf{K}',t-z)\mathcal{S}^*_{\mathbf{0},\mathbf{h}''}(\mathbf{K}',t-z)dz&\\ \times\frac{K'}{2}X_{\mathbf{h}'-\mathbf{h}'',\mathbf{g}'-\mathbf{g}''}(\mathbf{K},\mathbf{K}',E)d\Omega_{K'}.&\end{aligned} \tag{20}$$

Due to the finer sampling of reciprocal space in STEM calculations, they are much more computationally demanding than electron-diffraction spectroscopy simulations assuming plane-wave incidence. However, in STEM EELS imaging it is desirable to use a large detector collection angle to maximize the signal collected. Use of a large detector collection angle allows us to make a simplifying approximation, the so-called single-channeling approximation. If the detector is large enough to collect all of the energy loss electrons, then their redistribution due to elastic scattering subsequent to ionization does not affect the signal. Therefore we need not describe it in detail. This can be thought of as "turning off" the elastic potential subsequent to the ionization events, in which case the scattering matrix elements $\mathcal{S}_{\mathbf{0},\mathbf{g}''}(\mathbf{K}',t-z)=\delta_{\mathbf{0},\mathbf{g}''}$ (up to a phase factor which is irrelevant given we only measure intensities). Thus Eq. (20) simplifies to

$$\begin{aligned}\frac{\partial\sigma(\mathbf{R},t)}{\partial E}=NV_c\frac{2m}{\hbar^2K}\sum_{\mathbf{g}',\mathbf{h}'}\frac{1}{t}\int_0^t\sum_{\mathbf{g},\mathbf{h}}\mathcal{S}_{\mathbf{g}',\mathbf{g}}(\mathbf{K},z)T(\mathbf{g})e^{-2\pi i\mathbf{g}\cdot\mathbf{R}}&\\ \times\mathcal{S}^*_{\mathbf{h}',\mathbf{h}}(\mathbf{K},z)T^*(\mathbf{h})e^{2\pi i\mathbf{h}\cdot\mathbf{R}}dz&\\ \times\frac{K'}{2}\int X_{\mathbf{h}',\mathbf{g}'}(\mathbf{K},\mathbf{K}',E)d\Omega_{K'}.&\end{aligned} \tag{21}$$

Again making the dipole approximation and, for simplicity of notation, assuming $K$-shell ionization, this becomes

$$\begin{aligned}\frac{\partial\sigma(\mathbf{R},t)}{\partial E}=\frac{NV_c}{K\pi^2a_0^2}\sum_{n,\alpha,\beta}R_{n,\alpha\beta}(E)\sum_{\mathbf{g}',\mathbf{h}',\mathbf{g},\mathbf{h}}\frac{1}{t}&\\ \times\int_0^t\mathcal{S}_{\mathbf{g}',\mathbf{g}}(\mathbf{K},z)T(\mathbf{g})e^{-2\pi i\mathbf{g}\cdot\mathbf{R}}&\\ \times\mathcal{S}^*_{\mathbf{h}',\mathbf{h}}(\mathbf{K},z)T^*(\mathbf{h})e^{2\pi i\mathbf{h}\cdot\mathbf{R}}dz&\\ \times K'\int\mathcal{F}_n\frac{(\mathbf{q}+\mathbf{h}')_\alpha(\mathbf{q}+\mathbf{g}')_\beta}{|\mathbf{q}+\mathbf{h}'|^2|\mathbf{q}+\mathbf{g}'|^2}d\Omega_{K'},&\end{aligned} \tag{22}$$

where now

$$\mathcal{F}_n=e^{-0.25B_n(\mathbf{g}'-\mathbf{h}')}e^{2\pi i(\mathbf{g}'-\mathbf{h}')\cdot\tau_n}. \tag{23}$$

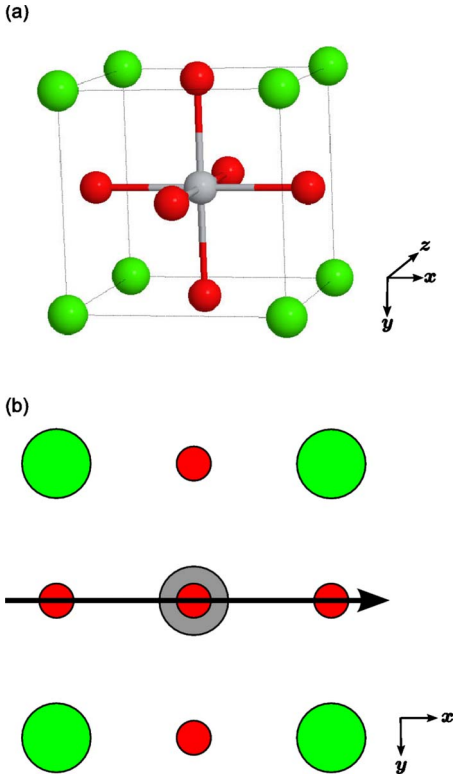


FIG. 10. (Color online) (a) Unit cell of $SrTiO_3$. The strontium atoms are shown in light gray (green), titanium in medium gray, and oxygen in dark gray (red). Created using JMOL (Ref. 75). (b) Projection of the unit cell of $SrTiO_3$ along [001]. The arrow indicates the scan direction of the probe.

Single-channeling simulations scale such as $g_{\max}^4$, where $g_{\max}$ is the maximum magnitude of the beams, **G**, included in the calculation. Double-channeling calculations scale such as $g_{\max}^8$. As such, in STEM we will only consider single channeling. For a detector with an acceptance angle larger than the probe-forming aperture this is a good approximation.[80]

## VI. CASE STUDY: FOCUSED COHERENT PROBE

The greatest benefit of using a focused coherent STEM probe to measures ELNES is that we can measure the change in fine structure, and hence in the local atomic environment, as we scan the probe across the sample. We explore this possibility in this section using $SrTiO_3$ as a case study.

### A. Structure of $SrTiO_3$

The structure of $SrTiO_3$ is depicted in Fig. 10(a). The local environment of the oxygen atom is dominated by the titanium bonds. This leads to the energy-differential cross section of the oxygen *K* shell being dichroic. In Fig. 10(b) the structure of $SrTiO_3$ projected along [001] is depicted. For the leftmost oxygen column the Ti-O-Ti bonds are in the direction of the arrow, i.e., along the *x* direction and in the plane of the page. In this case the relevant $R_{\alpha,\beta}$ in Eq. (22) (suppressing the index *n*) are $R_{yy}=R_{zz}\equiv R_\perp$, where $\perp$ denotes that these are directions perpendicular to the bonds, and $R_{xx}\equiv R_\parallel$, where $\parallel$ denotes directions parallel to the bonds. Now let us consider the column of atoms in the center. These O atoms have an identical local environment to the ones in the leftmost column but rotated by 90°. The Ti-O-Ti bonds are now down the column in the *z* direction or into the page. In this case $R_{xx}=R_{yy}=R_\perp$ and $R_{zz}=R_\parallel$.

If we only have momentum transfer in the *z* direction, as is the case for plane-wave illumination with an on-axis point detector, we would get $R_\perp$ contributions from the O only columns and $R_\parallel$ contributions from the central column due to the respective directions of the Ti-O-Ti bonds. For a focused coherent probe and a finite-size detector the situation becomes more complex since the momentum transfer now has components in the *x* and *y* directions. In this case we will then have $R_\perp$ and $R_\parallel$ contributions from all the oxygen atoms but in general weighted differently, depending on the probe and the channeling of the probe. For a sufficiently fine probe we would mainly excite one column and hence as we scan the probe we would expect to see some change in the fine structure as we encounter O columns with bonds orientated differently.[43] To get a feel for this and the effects of dynamical scattering we examine a simplified case. Rather than looking at the details of the fine structure we can simply look at the relative strength of the two spectra $R_\perp$ and $R_\parallel$ as a function of probe position. It suffices to only look at one energy, the threshold energy. As in the previous section, this is valid because the major effect of the channeling is to weight the different spectra. Again using the dipole approximation, our calculations fully include the detailed description of the ionization interaction, including the so-called nonlocality of the inelastic matrix elements and the partial coherence of the inelastically scattered wave field as it affects the signal reaching the detector. In the following calculations a $5\times5$ supercell was used. First we will explore the effects of the detector acceptance angle, then the size of the probe-forming aperture and then sample thickness and finally the change in fine structure as a function of probe position.

### B. Effect of detector acceptance angle

Calculations using a 100 keV aberration-free probe with a 20 mrad probe-forming aperture and a 100-Å-thick sample were performed for a range of detector apertures. In Fig. 11(a) we see the variation in the $R_\parallel$ component of the spectrum as we scan across the unit cell.

For the 10 mrad detector angle, most of the vectors **q** that will scatter into the detector have little component perpendicular to the beam direction. Also for the 10 mrad detector we see that the $R_\parallel$ signal is greatest in between the columns. In this case we are mostly detecting the signal from the O only column, but, with the probe on the column, the majority of inelastic scattering falls outside the very small detector considered here. Displacing the probe decreases the total inelastic-scattered intensity but may increase that portion reaching the detector. This gives rise to the characteristic volcano-shape image, as has been described previously.[32,81] This can make interpretation difficult as the image no longer represents the structure we are trying to image. As such it is best to avoid this regime. As we increase the probe (or de-

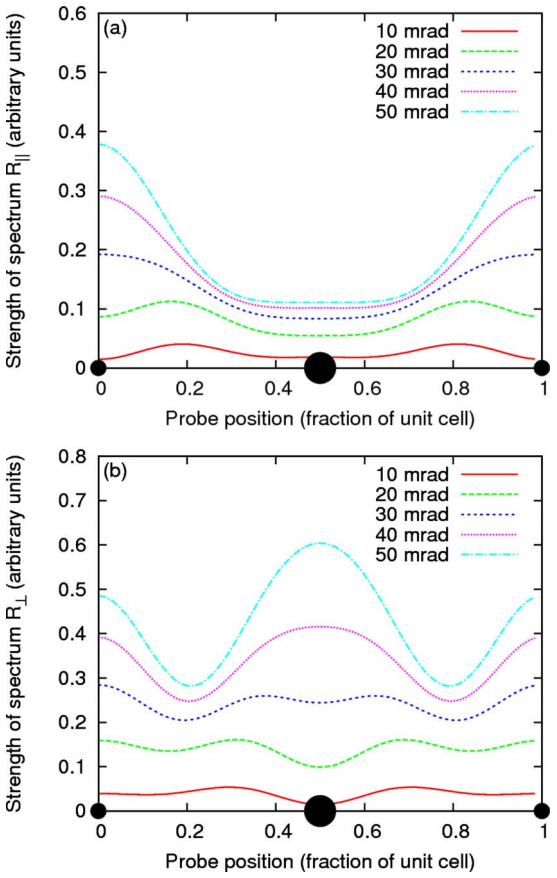


FIG. 11. (Color online) Simulation for a 100 keV aberration-free 20 mrad probe-forming aperture with a 100-Å-thick sample. (a) Strength of the $R_{\parallel}$ spectrum as a function of probe position for a range of detector sizes. (b) Strength of the $R_{\perp}$ spectrum as a function of probe position for a range of detector sizes. The small circles indicate O columns and the large circle indicates the Ti-O column.

tector) angle we allow scattering vectors **q** with a greater component perpendicular to the propagation of the fast electron and thus greater excitation of $R_{\parallel}$ for the O only columns, the more so as the aperture increases. The $z$ component of the momentum transfer, however, remains largely unchanged so that for the central column $R_{\parallel}$ mainly reflects an increase in signal due to the larger detector. In Fig. 11(b) we see again a volcano structure for the smallest detector apertures. As the aperture size increases, components of momentum transfer in the $x$ and $y$ directions increases. For the O only columns $R_{\perp}$ is excited along the $y$ and $z$ directions. For the Ti-O column, $R_{\perp}$ is excited by momentum transfers in the $x$ and $y$ direction. In this case the $R_{\perp}$ spectra from all atoms are affected by the increased range of momentum transfers as the aperture increases. Ideally we want to operate in a regime where the observed structure correlates with the atomic structure and as such large detectors are advantageous.

### C. Effect of probe-forming aperture

Calculations were performed for a 100 keV probe for a range of aberration-free probe-forming apertures. For the 10 and 20 mrad probe-forming aperture semiangles the calculation was found to converge with 121 physical reciprocal-lattice vectors. For the 30 mrad probe-forming aperture 305 reciprocal-lattice vectors were used, and 505 reciprocal lattice vectors were used for the 40 mrad probe-forming aperture. In the following calculations the sample was 100 Å thick.

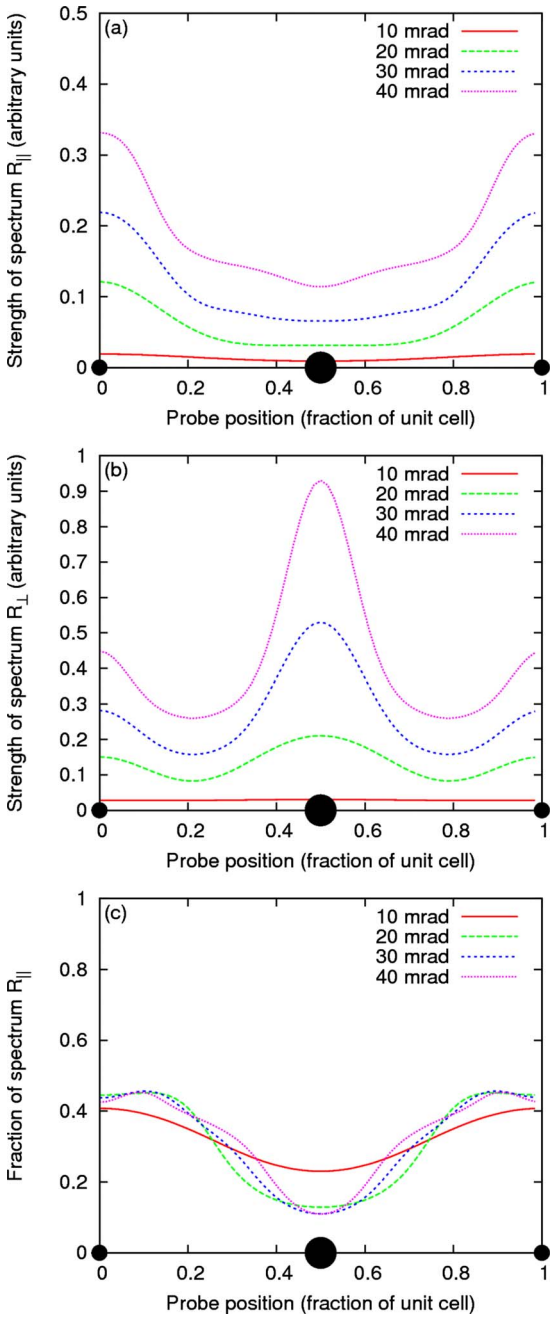


FIG. 12. (Color online) Simulation for an aberration-free probe with a 60 mrad detector acceptance angle and 100-Å-thick sample. (a) Strength of the $R_{\parallel}$ spectrum as a function of probe position for a range of probe-forming apertures. (b) Strength of the $R_{\perp}$ spectrum as a function of probe position for a range of probe-forming apertures. The small circles indicate O columns and the large circle indicates the Ti-O column.

In Fig. 12(a) we see how the strength of the $R_{\parallel}$ spectrum varies as we scan the probe along the direction indicated in

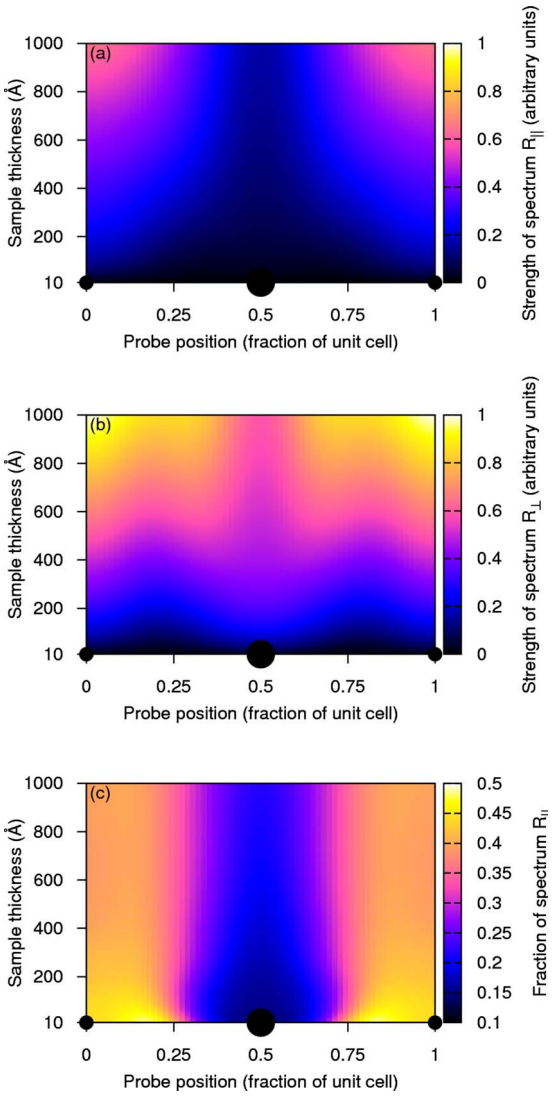


FIG. 13. (Color online) Simulation for an aberration-free 20 mrad probe with a 50 mrad detector acceptance angle. (a) Strength of the $R_{\parallel}$ spectrum as a function of probe position and sample thickness. (b) Strength of the $R_{\perp}$ spectrum as a function of probe position and sample thickness. (c) Fraction of the $R_{\parallel}$ spectrum of the total signal as a function of probe position and sample thickness. The small circles indicate O columns and the large circle indicates the Ti-O column.

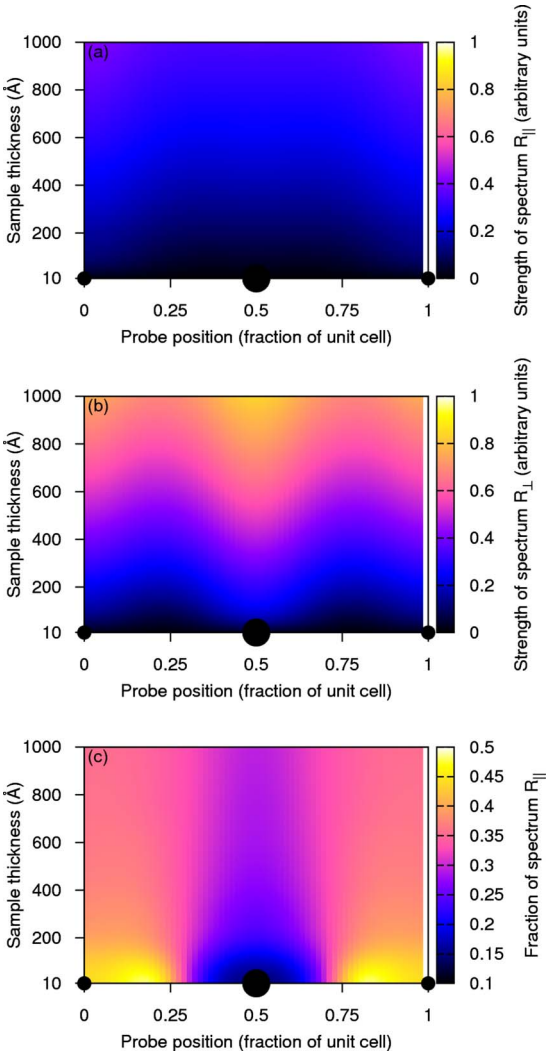


FIG. 14. (Color online) Same as Fig. 13 but with no channeling. The probe propagates in free space to the atoms in different layers.

Fig. 10(b) for a range of different probe-forming apertures with a 60 mrad detector. In Fig. 12(b) we show the $R_{\perp}$ spectrum. In this case, due to the large detector size, there is considerable sampling of transverse momentum transfers. In comparison to Fig. 11 we no longer see the volcano structure as the signal is peaked on the columns.

### D. Effect of sample thickness

Using an aberration-free probe with 20 mrad probe forming and 50 mrad detector aperture, calculations were performed to examine the change in O *K*-shell signal as a function of probe position and the thickness of the sample. In Fig. 13(a) the strength of the $R_{\parallel}$ spectrum is plotted. We can see the signal gradually increasing as the sample thickness increases, peaking on the O only columns. This peaking is enhanced by the channeling. To establish that it is genuinely the dynamical scattering in the specimen which causes this enhancement, Fig. 13(a) should be compared with Fig. 14(a), which is a similar calculation except that the elastic evolution of the incident wave field is assumed to occur in free-space rather than in the crystal potential. The strength of the $R_{\perp}$ spectrum is plotted in Fig. 13(b). It can be seen that the signal builds up more quickly than in Fig. 13(a), which is on the same scale. Once again, channeling plays an important role, leading to maxima on the O only columns. This should be contrasted with the results in Fig. 14(b), where the maximum intensity is on the central Ti-O column for larger thicknesses. In Fig. 13(c) we see the fraction of the signal from the $R_{\parallel}$ spectrum as a function of probe position and thickness. The greatest variation as a function of probe position is seen for the smallest thicknesses, but, as the thicker specimens produce a greater absolute signal strength, the thicker samples are most likely advantageous for detecting the changes in fine structure. We also note that channeling (and

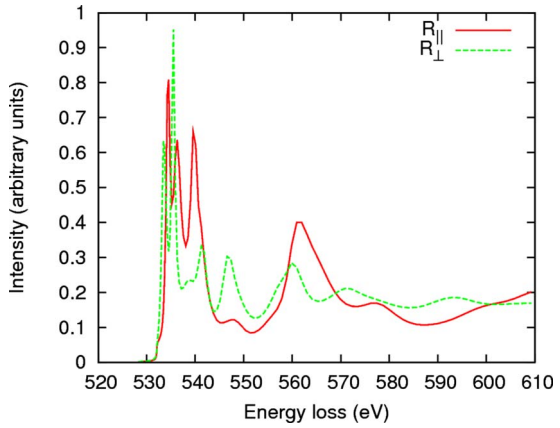


FIG. 15. (Color online) Oxygen $K$-edge spectra in the dipole approximation for $SrTiO_3$. The spectrum $R_{\|}$ is associated with scattering vector in the direction of the titanium-oxygen bonds of the ionized atom and the spectrum $R_{\perp}$ is associated with scattering vector perpendicular to the titanium-oxygen bonds of the ionized atom.

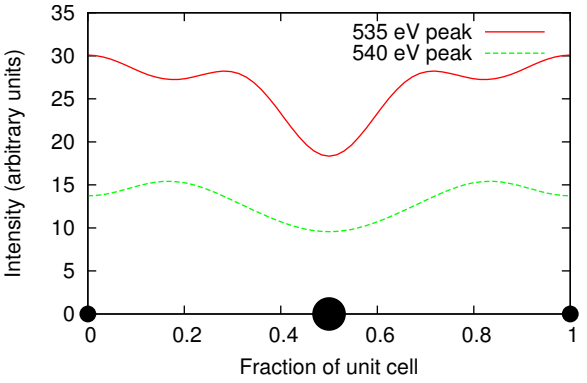


FIG. 17. (Color online) STEM ELNES cross section for the O $K$ edge in $SrTiO_3$ as a function of probe position for energy losses of 535 eV (solid red line) and 540 eV (dotted green line). The probe-forming and detector-acceptance angles are both 20 mrad. The probe has been scanned from an oxygen column to a titanium-oxygen column and back to an oxygen column in the (001) zone axis, as indicated in Fig. 10. The small circles indicate O columns and the large circle indicates the Ti-O column.

absorption) preserves the contrast for thicker specimens, as can be seen by comparing with Fig. 14(c). Having explored the effect of some of the most pertinent experiment parameters we now turn our attention toward simulating the full ELNES spectra.

### E. Fine structure as a function of probe position

In Fig. 15 we can see the two different STEM ELNES spectra from the oxygen atom, $R_{\|}$ associated with the direction of the titanium-oxygen bonds of the ionized atom and $R_{\perp}$ associated with directions perpendicular to this. These spectra were calculated using FEFF with a cluster of radius 6.0 Å around the ionized atom and the potentials calculated self-consistently within a radius of 4.5 Å. As can be seen, there are marked differences between the spectra, particularly at energy losses of around 540 and 547 eV.

These spectra were then used to calculate the energy-differential cross section as a function of probe position, scanning across from an oxygen column to a titanium-oxygen column and back to an oxygen column, as indicated by the arrow in Fig. 10. A 100 keV probe was assumed. The probe-forming aperture and detector acceptance angles were both 20 mrad, values easily obtained not only on the latest generation of aberration-corrected microscopes but also on earlier models. The result is seen in Fig. 16. The changes in the fine structure are more evident in Fig. 17, where we compare the heights of the peaks at 535 and 540 eV as a function of probe position. The two peaks quite clearly have different behavior as we scan across the unit cell, evidence of the change in fine structure as a function of probe position. While our present calculations do not allow for broadening in the energy direction due to thermal effects and the finite lifetime of the ejected electron, we can see that, in principle, we should be able to measure a change in the fine structure at atomic scales using the latest scanning transmission electron microscopes. As discussed in the previous section, using larger probe-forming and detector apertures will improve these results.

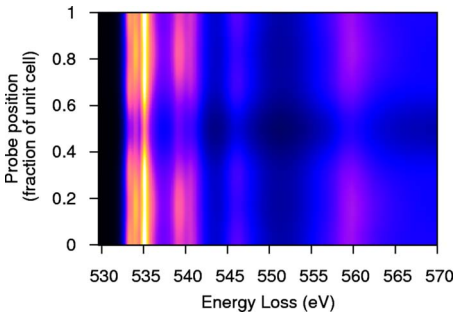


FIG. 16. (Color online) STEM ELNES cross section for the O $K$ edge in $SrTiO_3$ as a function of probe position and energy loss in arbitrary units. The probe-forming and detector-acceptance angles are both 20 mrad. The probe is scanned from an oxygen column to a titanium-oxygen column and back to an oxygen column in the (001) zone axis as indicated in Fig. 10.

## VII. CONCLUSION

Dynamical scattering can be used to concentrate the probe density on specific sites within the unit cell. This can be used to identify the atomic species occupying different lattice sites. Furthermore this can be used to probe the fine structure in the energy loss spectra of the atoms on different sites. Increasing the size of the detector makes the energy loss interactions more local leading to a greater change in the spectra as a function of sample tilt. Alternatively, offsetting the detector can achieve similar results but at the cost of greater statistical noise due to the reduction in signal strength. Combining the calculations of fine structure from

the FEFF program, full double-channeling including ELNES have been simulated. We have compared our simulation with experiment and found that we have reliably reproduced peak locations and the general change in the peak heights as the sample is tilted but have not reproduced the exact peak heights.

We have presented the theory of ELNES imaging in STEM. We have seen how STEM can be used to measure how fine structure, and hence the local density of unoccupied states, changes at atomic scales. In particular, we have demonstrated how in $SrTiO_3$ the measured oxygen $K$ edge changes as a function of probe position within the unit cell.

**ACKNOWLEDGMENTS**

The authors would like to thank Z. Levine, K. Jorissen, and A. Sorini for helpful discussions from their independent explorations of generalizing the FEFF code for the calculation of MDFFs. L.J.A. acknowledges support from the Australian Research Council. S.D.F. is supported by the Japan Society for the Promotion of Science (JSPS). This research was sponsored by the Office of Basic Energy Sciences, Division of Materials Sciences and Engineering, U.S. Department of Energy, under Contract No. DE-AC05-00OR22725 with Oak Ridge National Laboratory, managed and operated by UT-Battelle, LLC.

[1] M. Varela, S. D. Findlay, A. R. Lupini, H. M. Christen, A. Y. Borisevich, N. Dellby, O. L. Krivanek, P. D. Nellist, M. P. Oxley, L. J. Allen, and S. J. Pennycook, Phys. Rev. Lett. **92**, 095502 (2004).
[2] E. Okunishi, H. Sawada, J. Kondo, and M. Kersker, Microsc. Microanal. **12**, 1150 (2006).
[3] M. Bosman, V. J. Keast, J. L. Garcia-Munoz, A. J. D'Alfonso, S. D. Findlay, and L. J. Allen, Phys. Rev. Lett. **99**, 086102 (2007).
[4] K. Kimoto, T. Asaka, T. Nagai, M. Saito, Y. Matsui, and K. Ishizuka, Nature (London) **450**, 702 (2007).
[5] D. A. Muller, L. F. Kourkoutis, M. Murfitt, J. H. Song, H. Y. Hwang, J. Silcox, N. Dellby, and O. L. Krivanek, Science **319**, 1073 (2008).
[6] L. J. Allen, Nat. Nanotechnol. **3**, 255 (2008).
[7] P. Rez, J. Bruley, P. Brohan, M. Payne, and L. A. J. Garvie, Ultramicroscopy **59**, 159 (1995).
[8] V. J. Keast, A. J. Scott, R. Brydson, D. B. Williams, and J. Bruley, J. Microsc.-Oxford **203**, 135 (2001).
[9] O. L. Krivanek, M. M. Disko, J. Taftø, and J. C. H. Spence, Ultramicroscopy **9**, 249 (1982).
[10] M. S. Moreno, K. Jorissen, and J. J. Rehr, Micron **38**, 1 (2007).
[11] R. F. Egerton, *Electron Energy-Loss Spectroscopy in the Electron Microscope* (Plenum, New York, 1996).
[12] P. Rez, J. R. Alvarez, and C. Pickard, Ultramicroscopy **78**, 175 (1999).
[13] J. J. Rehr and A. L. Ankudinov, Coord. Chem. Rev. **249**, 131 (2005).
[14] P. Rez and D. A. Muller, Annu. Rev. Mater. Res. **38**, 535 (2008).
[15] J. A. Soininen, A. L. Ankudinov, and J. J. Rehr, Phys. Rev. B **72**, 045136 (2005).
[16] P. Blaha, K. Schwarz, P. Sorantin, and S. Trickey, Comput. Phys. Commun. **59**, 399 (1990).
[17] VASP *homepage*, http://cms.mpi.univie.ac.at/vasp/
[18] Y. Joly, Phys. Rev. B **63**, 125120 (2001).
[19] N. D. Browning, J. Yuan, and L. M. Brown, Ultramicroscopy **38**, 291 (1991).
[20] N. K. Menon and J. Yuan, Ultramicroscopy **74**, 83 (1998).
[21] N. K. Menon and J. Yuan, Ultramicroscopy **78**, 185 (1999).
[22] M. Nelhiebel, P. H. Louf, P. Schattschneider, P. Blaha, K. Schwarz, and B. Jouffrey, Phys. Rev. B **59**, 12807 (1999).
[23] C. Hébert-Souche, P.-H. Louf, P. Blaha, M. Nelheibel, J. Luitz, P. Schattschneider, K. Schwarz, and B. Jouffrey, Ultramicroscopy **83**, 9 (2000).
[24] C. Heiliger, F. Heyroth, F. Syrowatka, H. S. Leipner, I. Maznichenko, K. Kokko, W. Hergert, and I. Mertig, Phys. Rev. B **73**, 045129 (2006).
[25] J. C. H. Spence and J. Taftø, J. Microsc. **130**, 147 (1983).
[26] J. Taftø, Micron **34**, 157 (2003).
[27] D. K. Saldin, Philos. Mag. B **56**, 515 (1987).
[28] P. Schattschneider, C. Hébert, and B. Jouffrey, Ultramicroscopy **86**, 343 (2001).
[29] Y. Yamamoto, K. Tatsumi, and S. Muto, Mater. Trans. **48**, 2590 (2007).
[30] K. Tatsumi, S. Muto, Y. Yamamoto, H. Ikeno, S. Yoshioka, and I. Tanaka, Ultramicroscopy **106**, 1019 (2006).
[31] S. Arai, S. Muto, T. Sasaki, K. Tatsumi, Y. Ukyo, K. Kuroda, and H. Saka, Solid State Commun. **135**, 664 (2005).
[32] H. Kohl and H. Rose, Adv. Imaging Electron Phys. **65**, 173 (1985).
[33] V. W. Maslen and C. J. Rossouw, Philos. Mag. A **49**, 735 (1984).
[34] C. J. Rossouw and V. M. Maslen, Philos. Mag. A **49**, 743 (1984).
[35] D. K. Saldin and P. Rez, Philos. Mag. B **55**, 481 (1987).
[36] L. J. Allen, S. D. Findlay, M. P. Oxley, and C. J. Rossouw, Ultramicroscopy **96**, 47 (2003).
[37] L. J. Allen, Ultramicroscopy **48**, 97 (1993).
[38] L. J. Allen and T. W. Josefsson, Phys. Rev. B **52**, 3184 (1995).
[39] M. P. Oxley and L. J. Allen, Acta Crystallogr., Sect. A: Found. Crystallogr. **57**, 713 (2001).
[40] D. A. Muller and J. Silcox, Ultramicroscopy **59**, 195 (1995).
[41] M. P. Oxley, E. C. Cosgriff, and L. J. Allen, Phys. Rev. Lett. **94**, 203906 (2005).
[42] G. Möbus and S. Nufer, Ultramicroscopy **96**, 285 (2003).
[43] T. Mizoguchi, J. P. Buban, K. Matsunaga, T. Yamamoto, and Y. Ikuhara, Ultramicroscopy **106**, 92 (2006).
[44] P. Schattschneider, M. Nelhiebel, and B. Jouffrey, Phys. Rev. B **59**, 10959 (1999).
[45] M. P. Oxley and L. J. Allen, Acta Crystallogr., Sect. A: Found. Crystallogr. **56**, 470 (2000).
[46] J. Verbeeck, P. Schattschneider, and A. Rosenauer, Ultramicroscopy **109**, 350 (2009).
[47] D. K. Saldin and J. M. Yao, Phys. Rev. B **41**, 52 (1990).
[48] D. K. Saldin and Y. Ueda, Phys. Rev. B **46**, 5100 (1992).
[49] Y. Ueda and D. K. Saldin, Phys. Rev. B **46**, 13697 (1992).

[50] R. D. Leapman and J. Silcox, Phys. Rev. Lett. **42**, 1361 (1979).
[51] R. D. Leapman, P. L. Fejes, and J. Silcox, Phys. Rev. B **28**, 2361 (1983).
[52] B. Jouffrey, P. Schattschneider, and C. Hébert, Ultramicroscopy **102**, 61 (2004).
[53] P. Schattschneider, C. Hébert, H. Franco, and B. Jouffrey, Phys. Rev. B **72**, 045142 (2005).
[54] J. C. Le Bossé, T. Épicier, and B. Jouffrey, Ultramicroscopy **106**, 449 (2006).
[55] C. Hébert, P. Schattschneider, H. Franco, and B. Jouffrey, Ultramicroscopy **106**, 1139 (2006).
[56] C. Brouder, M. F. Ruiz López, R. F. Pettifer, M. Benfatto, and C. R. Natoli, Phys. Rev. B **39**, 1488 (1989).
[57] C. Brouder, J. Phys.: Condens. Matter **2**, 701 (1990).
[58] J. C. Le Bossé, T. Épicier, and H. Chermette, Phys. Rev. B **76**, 075127 (2007).
[59] A. L. Ankudinov, B. Ravel, J. J. Rehr, and S. D. Conradson, Phys. Rev. B **58**, 7565 (1998).
[60] L. Dagum and R. Menon, IEEE Comput. Sci. Eng. **5**, 46 (1998).
[61] C. J. Humphreys, Rep. Prog. Phys. **42**, 1825 (1979).
[62] C. Dwyer, Phys. Rev. B **72**, 144102 (2005).
[63] C. Dwyer and J. S. Barnard, Phys. Rev. B **74**, 064106 (2006).
[64] L. J. Allen, S. D. Findlay, M. P. Oxley, C. Witte, and N. J. Zaluzec, Phys. Rev. B **73**, 094104 (2006).
[65] F. Fujimoto, J. Phys. Soc. Jpn. **14**, 1558 (1959).
[66] L. Sturkey, Proc. Phys. Soc. London **80**, 321 (1962).
[67] T. W. Josefsson and L. J. Allen, Phys. Rev. B **53**, 2277 (1996).
[68] W. Coene and D. Van Dyck, Ultramicroscopy **33**, 261 (1990).
[69] S. L. Dudarev, L. M. Peng, and M. J. Whelan, Phys. Rev. B **48**, 13408 (1993).
[70] L. J. Allen, S. D. Findlay, M. P. Oxley, C. Witte, and N. J. Zaluzec, Ultramicroscopy **106**, 1001 (2006).
[71] M. P. Oxley and L. J. Allen, Phys. Rev. B **57**, 3273 (1998).
[72] J. Taftø and O. L. Krivanek, Phys. Rev. Lett. **48**, 560 (1982).
[73] J. Taftø, Nucl. Instrum. Methods Phys. Res. B **2**, 733 (1984).
[74] K. Tatsumi, T. Mizoguchi, S. Yoshioka, T. Yamamoto, T. Suga, T. Sekine, and I. Tanaka, Phys. Rev. B **71**, 033202 (2005).
[75] JMOL*: An Open-Source Java Viewer for Chemical Structures in 3D*, http://www.jmol.org/
[76] K. E. Sickafus, J. M. Wills, and N. W. Grimes, J. Am. Ceram. Soc. **82**, 3279 (1999).
[77] J. N. Roelofsen, R. C. Peterson, and M. Raudsepp, Am. Mineral. **77**, 522 (1992).
[78] E. J. Kirkland, R. F. Loane, and J. Silcox, Ultramicroscopy **23**, 77 (1987).
[79] J. C. H. Spence and J. M. Cowley, Optik (Jena) **50**, 129 (1978).
[80] S. D. Findlay, M. P. Oxley, and L. J. Allen, Microsc. Microanal. **14**, 48 (2008).
[81] A. J. D'Alfonso, S. D. Findlay, M. P. Oxley, and L. J. Allen, Ultramicroscopy **108**, 677 (2008).